Applied Physics Letters

Pair-partitioned bulk localized states induced by topological band inversion

Cite as: Appl. Phys. Lett. **121**, 011103 (2022); https://doi.org/10.1063/5.0101925
Submitted: 04 June 2022 • Accepted: 20 June 2022 • Published Online: 06 July 2022

Peng Peng, Exian Liu, Bei Yan, et al.

Applied Physics Letters ARTICLE scitation.org/journal/apl

Pair-partitioned bulk localized states induced by topological band inversion

Cite as: Appl. Phys. Lett. **121**, 011103 (2022); doi: 10.1063/5.0101925
Submitted: 4 June 2022 · Accepted: 20 June 2022 ·
Published Online: 6 July 2022

Peng Peng, Exian Liu, Bei Yan, Yuchen Peng, Aoqian Shi, Jianlan Xie, Hang Li, Yuanjiang Xiang, and Jianjun Liu[a)]

AFFILIATIONS

Key Laboratory for Micro/Nano Optoelectronic Devices of Ministry of Education & Hunan Provincial Key Laboratory of Low-Dimensional Structural Physics and Devices, School of Physics and Electronics, Hunan University, Changsha 410082, China

[a)]Author to whom correspondence should be addressed: jianjun.liu@hnu.edu.cn

ABSTRACT

Photonic topological insulators have recently received widespread attention mainly due to their ability to provide directions in the development of photonic integration platforms. The proposal for a topological bulk cavity with a single-mode expands upon previous research works on topological cavities; thus, interest in topological edge states and corner states is beginning to shift into analysis on bulk properties and their applications. However, there remains a gap in research on a multi-mode cavity of the topological photonic crystals (PCs). In this Letter, a cavity of the topological PCs is proposed involving pair-partitioned bulk localized states (BLSs) from a two-dimensional inner and outer nested square lattice (2D IONSL), which can enable a multi-mode cavity for the topological PCs. First, the topological characteristics are described in terms of a Zak phase, and band inversions are achieved by changing the size of scatterers in the inner and outer circles that reside within the unit cell. Afterwards, analogous to the tight-binding model for electronic systems, the Hamiltonian and topological phase transition conditions of 2D IONSL PCs are derived. Furthermore, it is proposed that the demonstrated optical field reflection and confinement mechanism induced by topological band inversions due to the opposite parities of wavefunctions may lead to the phenomenon of pair-partitioned BLSs. This research increases the research works of bulk topological effects, creating a route for photonic integration platforms for near-infrared.

Topological insulators are widely studied materials because of their unique defect-immune and unidirectional backscattering-immune characteristics. These factors provide a methodology that can improve the transmission distance and the efficiency of traditional integrated devices.[1–3] Inspired by the idea of topological insulators in electrons, such a concept of topology was gradually extended to other systems, including photonics,[4,5] phonics,[6,7] and cold atom systems.[8] As the research on topological physics continually advances, the photonic quantum spin Hall effect,[9,10] photonic topological insulator,[11,12] and topological semimetals[13,14] have been regularly proposed and, to some extent, proven by experiments. Topological photonics has become of great interest since the subject can provide methods for manipulating optical fields and can be applied to a broad range of prospects such as an optical isolator,[15] a beam splitter,[16] an optical coupler,[17,18] and other devices. In recent years, research on topological photonics has especially arisen in the field of higher-order topological insulators that break the conventional bulk-edge correspondence.[4,5,19–28]

In addition, there have been many interesting recent studies on photonics in the cavity of topological photonic crystals (PCs) based on edge states and corner states.[22,29–34] In 2020, Shao *et al.* produced a topological bulk cavity with topological non-trivial state (TNS) PCs that are surrounded by topological trivial state (TTS) PCs, which is based on a band-inversion-induced reflection and confinement mechanism in the whole non-trivial region.[35] This previous work extended research from edge states and corner states to bulk localized states (BLSs), which opened up a prelude for research on bulk cavities and their applications, i.e., in terms of producing a topological bulk laser. The PC resonator laser, which acts as an enhancer of spontaneous emission, can be constructed based on defect states and ideal optical field reflection characteristics. The proposal for a topological bulk cavity with single-mode expands upon previous research on topological cavities; thus, interest in topological edge states and corner states is beginning to shift into analyzes on bulk properties and their applications such as single-mode vertical-cavity surface-emitting lasers (VCSELs). Compared to single-mode lasing, multi-mode VCSELs

have been the dominant components in short-reach links and high-performance computing applications owing to their low cost, low modal noise, and low power consumption.[36–38] However, there is still a gap in research on multi-mode VCSELs, and cavity design is crucial for VCSELs; so, an exploration of the multi-mode cavity of the topological PCs is required. In general, topological photonics is based on either square lattices,[4,7,8,20,23,32,34,39–41] Stampfli-triangle PCs,[9,42] honeycomb lattices,[10–12,34,43,44] or kagome lattices.[19,24] Yet, in order to enrich the PC structure and provide more platforms for research on its topological physics, construction of a type of PC is required.

In this Letter, a form of PC is constructed based upon a two-dimensional inner and outer nested square lattice (2D IONSL). The relationship between the size of the scatterers within the unit cell of the PC and the topological phase transition is determined via relevant expressions, and the results are analyzed. The Hamiltonian and topological phase transition conditions of the 2D IONSL PC are theoretically derived from the tight-binding model of the electronic system. Based on the cavity of PCs with a box-shaped structure, the edge states, corner states, and BLSs are realized, and they correspond to the band structure one-by-one. The optical field is reflected at the topological interface, forming an effective cavity feedback for lasing. It is proposed that the optical field reflection and confinement mechanism induced by topological band inversions can be demonstrated. This leads to the phenomenon known as pair-partitioned BLSs, becoming realized in the simulation. The relationship between the eigenfrequency and the distribution of the pair-partitioned BLSs is also analyzed.

The unit cell, the band structure of the 2D IONSL PC, and density of states (DOSs) are shown in Fig. 1. Here, α and β are square lattices with different radii that are nested together around the geometric center of a 2D IONSL PC. Moreover, the lattice constant is represented by a, and the material used in the scatterers is silicon (permittivity, $\varepsilon_1 = 12$), which is surrounded by air ($\varepsilon_2 = 1$). The radii of the scatterers for α and β square lattices are r_1 and r_2, respectively, and the relevant distances for each are $2l_1$ and $2l_2$ in Fig. 1(a), respectively.

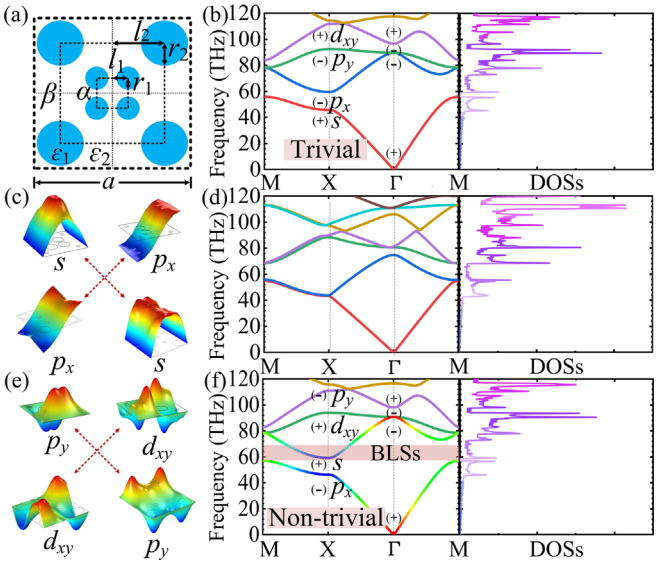

FIG. 1. (a) Schematic for the 2D IONSL PC, in which $a = 1.5\,\mu$m, $l_1 = 0.14a$, $l_2 = 0.356a$, $\varepsilon_1 = 12$, and $\varepsilon_2 = 1$. Graphs showing the band structure and DOSs when (b) $r_1 = 0.12a$ and $r_2 = 0.06a$ (for $\gamma = 2$), (d) $r_1 = r_2 = 0.12a$ ($\gamma = 1$), and (f) $r_1 = 0.06a$ and $r_2 = 0.12a$ ($\gamma = 1/2$). In (f), the shaded area depicts the pair-partitioned BLSs. Contour maps of the electric fields of the first, second, third, and fourth bands at the X point, where (c) $\gamma = 2$ and (e) $\gamma = 1/2$. The parity can be judged from the electric fields; + and − represent the even and odd parity, respectively, as seen in (b) and (f).

The ratio $\gamma = r_1/r_2$, which relates the radius of the scatterers of the inner and outer circles in the 2D IONSL PC, is a key parameter used to characterize the topological phase transition. As shown in Figs. 1(b), 1(d), and 1(f), when γ changes from 2 to 1 and then to 1/2, the Dirac point experiences a process from opening to closing to opening again. The electric fields at the X point in Figs. 1(b) and 1(f) are shown in Figs. 1(c) and 1(e), respectively; the first, second, third, and fourth bands are the s, p_x, p_y, and d_{xy} and the p_x, s, d_{xy}, and p_y, respectively, for each figure. It is clearly seen that the first and second bands (and the third and fourth bands) are inverted when γ is continually adjusted from 2 to 1/2. The inversion of the s and p_x between the first and second bands (or the p_y and d_{xy} between the third and fourth bands) indicates that the system can experience a topological phase transition.[4,45] In addition, such a transition is related to the bulk polarization, a relationship which can be described via

$$P = \frac{1}{2\pi}\int\int_{1\text{st BZ}} \mathrm{d}k_x \mathrm{d}k_y \,\mathrm{Tr}[A], \tag{1}$$

where $A = i\langle\mu_d|\partial_k|\mu_e\rangle$ is the Berry connection of the first Brillouin zone, in which d and e traverse bands below the photonic bandgap (PBG), and $|\mu_e\rangle$ is the Bloch function for the eth band. The value of the bulk polarization P is restricted by the C_4 symmetry and the time-reversal symmetry of the 2D IONSL, which can be determined by the X and Γ point parity symmetry (the eigenvalues of the inversion symmetry operator), so that[46]

$$P_j = \frac{1}{2}\left(\sum_e q_j^e \ \text{modulo}\ 2\right), \quad (-1)^{q_j^e} = \frac{\eta(\mathrm{X}_j)}{\eta(\Gamma)}, \tag{2}$$

where j represents the x or y direction, q_j^e is a topological invariant of the eth band, and its value is either 0 or 1. Moreover, X_j represents the X or Y points of the first Brillouin zone, and $\eta(\mathrm{X}_j)$ [or $\eta(\Gamma)$] is the parity at the X_j (or Γ) point; $P = (P_x, P_y)$ can be accurately quantized as 0 or 1/2, since the 2D IONSL PC has a time-reversal symmetry and a spatial inversion symmetry simultaneously. The bulk polarizations $P = (0, 0)$ and $P = (1/2, 1/2)$ represent the TTS and TNS, as shown in Figs. 1(b) and 1(f), respectively.

The existence of the vector Zak phase relates to the bulk polarization, which can be described with $\sigma_j = 2\pi p_j$ or $\sigma_j = 0$ or π under the constraint of the inversion symmetry. Therefore, $\sigma_j = (0, 0)$ corresponding to the case where $\gamma = 2$ is a TTS, while $\sigma_j = (\pi, \pi)$ relates to $\gamma = 1/2$ as a TNS.

For visualization of bands, we solve for their DOSs. The DOSs of PCs are the number of eigenstates in a unit frequency range, which can usually be expressed as[47,48]

$$N(F) = \sum_n \int_{BZ} \mathrm{d}^2k\,\delta[F - F_n], \tag{3}$$

where $\delta[F - F_n]$ represents the extraction of eigenstates at the same frequency. The solved DOSs' distributions are shown in the right part

of Figs. 1(b), 1(d), and 1(f). It can be found that the flatter the band, the sharper is the DOSs value, whereas the steeper the band, the lower is the peak of the DOSs. The DOSs' value at the PBG is 0, and the PBG here is narrower.

The physical origin of the topological can be explained by the tight-binding model, as shown in Fig. 2. The Hamiltonian of the 2D IONSL PC can be derived based on the tight-binding model. Since the coupling strength is identical for cases when the distances and the sizes are the same in the outer circles (or the inner circles), the four scatterers in the outer circles can be described by b_1, b_2, b_3, and b_4 in the counterclockwise directions. Furthermore, without loss of generality, the four scatterers in the inner circles are described as c_1, c_2, c_3, and c_4, which is shown in Fig. 2(a).

The theoretical analysis is now extended from the Su–Schrieffer–Heeger model of an electronic system to a photonic scheme. The eigenequation of a PC for the transverse magnetic (TM) modes can be written as[49]

$$\nabla \times \frac{1}{\varepsilon_{(\boldsymbol{r})}} \nabla \times \boldsymbol{\mu}_{e,\boldsymbol{k}}(\boldsymbol{r}) = \frac{w^2}{c^2} \boldsymbol{\mu}_{e,\boldsymbol{k}}(\boldsymbol{r}), \tag{4}$$

where the Hamiltonian of the photon is $\nabla \times \frac{1}{\varepsilon_{(r)}} \nabla \times$, while $\boldsymbol{\mu}_{e,\boldsymbol{k}}(\boldsymbol{r})$ is the Bloch function of the magnetic field and the eigenvalue is w^2/c^2. Analogous to the electronic system, the Hamiltonian of the photonic system can be decomposed as follows:

$$H = H_{\text{intra}} + H_{\text{inter}}, \tag{5}$$

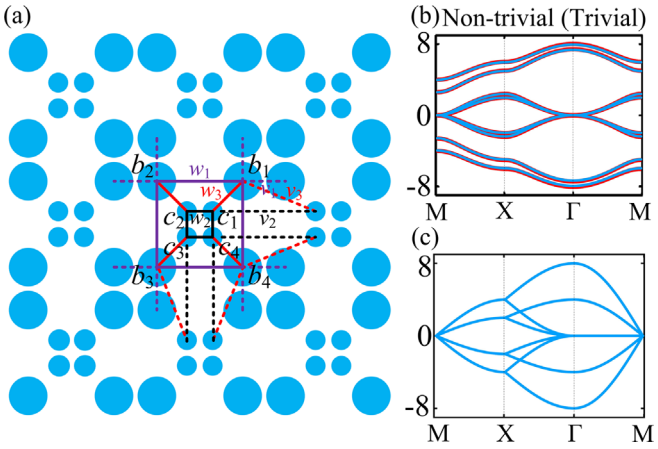

FIG. 2. (a) 2D Su–Schrieffer–Heeger model, in which the purple, black, and red solid lines represent the intra-cell coupling strengths between the two outer circles, the two inner circles, and the inner circles and outer circles in the same unit cell; these are labeled w_1, w_2, and w_3, respectively. The purple dashed lines represent the inter-cell coupling strength v_1 between the outer circles and the nearest outer circles, while the black dashed lines signify the coupling strength v_2 between the inner circles and the nearest inner circles. In addition, the red dashed lines depict the coupling strength v_3 between the outer circles and the nearest inner circles (which is equivalent to the inner circles and the nearest outer circles). (b) Graph for the overlapping and consistent TNS (where $w_1 = 1.2$, $v_1 = 2.5$, $w_2 = 3$, and $v_2 = 1$) and TTS ($w_1 = 2.5$, $v_1 = 1.2$, $w_2 = 1$, and $v_2 = 3$), which are shown as blue and red bold lines, respectively. (c) The case for $w_1 = v_1 = 2$ and $w_2 = v_2 = 1$.

where the intra-cell coupling Hamiltonian, H_{intra}, can be described via the coupling strengths w_1, w_2, and w_3. Thus, the following equation can be derived as

$$\begin{aligned} H_{\text{intra}} = \sum_{m,n}^{N} \Big[& w_1 (b_{1_{m,n}}^{\dagger} b_{2_{m,n}} + b_{2_{m,n}}^{\dagger} b_{3_{m,n}} + b_{3_{m,n}}^{\dagger} b_{4_{m,n}} + b_{4_{m,n}}^{\dagger} b_{1_{m,n}} + h.c.) \\ & + w_2 (c_{1_{m,n}}^{\dagger} c_{2_{m,n}} + c_{2_{m,n}}^{\dagger} c_{3_{m,n}} + c_{3_{m,n}}^{\dagger} c_{4_{m,n}} + c_{4_{m,n}}^{\dagger} c_{1_{m,n}} + h.c.) \\ & + w_3 (b_{1_{m,n}}^{\dagger} c_{1_{m,n}} + b_{2_{m,n}}^{\dagger} c_{2_{m,n}} + b_{3_{m,n}}^{\dagger} c_{3_{m,n}} + b_{4_{m,n}}^{\dagger} c_{4_{m,n}} + h.c.) \Big]. \end{aligned} \tag{6}$$

In addition, the explicit form of the inter-cell coupling Hamiltonian, H_{inter}, can be expressed by using the coupling strengths v_1, v_2, and v_3,

$$\begin{aligned} H_{\text{inter}} = \sum_{m,n}^{N} \Big[& v_1 (b_{1_{m,n}}^{\dagger} b_{2_{m+1,n}} + b_{4_{m,n}}^{\dagger} b_{3_{m+1,n}} + b_{4_{m,n}}^{\dagger} b_{1_{m,n+1}} \\ & + b_{3_{m,n}}^{\dagger} b_{2_{m,n+1}} + h.c.) + v_2 (c_{1_{m,n}}^{\dagger} c_{2_{m+1,n}} + c_{4_{m,n}}^{\dagger} c_{3_{m+1,n}} \\ & + c_{4_{m,n}}^{\dagger} c_{1_{m,n+1}} + c_{3_{m,n}}^{\dagger} c_{2_{m,n+1}} + h.c.) \\ & + v_3 (b_{1_{m,n}}^{\dagger} c_{2_{m+1,n}} + c_{1_{m,n}}^{\dagger} b_{2_{m+1,n}} + c_{4_{m,n}}^{\dagger} b_{3_{m+1,n}} + b_{4_{m,n}}^{\dagger} c_{3_{m+1,n}} \\ & + c_{4_{m,n}}^{\dagger} b_{1_{m,n+1}} + b_{4_{m,n}}^{\dagger} c_{1_{m,n+1}} + c_{3_{m,n}}^{\dagger} b_{2_{m,n+1}} + b_{3_{m,n}}^{\dagger} c_{2_{m,n+1}} + h.c.) \Big], \end{aligned} \tag{7}$$

where m (or n) represents the mth (or the nth) unit cell of the 2D IONSL PC array and *h.c.* signifies the Hermitian conjugate of the previous terms. The total Hamiltonian can be obtained as an 8×8 matrix by use of a Fourier transform, which can then be simplified to a 2×2 matrix

$$H(\mathbf{k}) = \begin{pmatrix} M_1 & N \\ N^* & M_2 \end{pmatrix}, \tag{8}$$

within which are the matrices

$$M_\tau = \begin{pmatrix} 0 & w_\tau + v_\tau e^{ik_x a} & 0 & w_\tau + v_\tau e^{-ik_y a} \\ w_\tau + v_\tau e^{-ik_x a} & 0 & w_\tau + v_\tau e^{-ik_y a} & 0 \\ 0 & w_\tau + v_\tau e^{ik_y a} & 0 & w_\tau + v_\tau e^{-ik_x a} \\ w_\tau + v_\tau e^{ik_y a} & 0 & w_\tau + v_\tau e^{ik_x a} & 0 \end{pmatrix}, \tag{9}$$

$$N = \begin{pmatrix} w_3 & v_3 (e^{ik_x a} + e^{-ik_y a}) & 0 & 0 \\ v_3 e^{-ik_x a} & w_3 & v_3 e^{-ik_y a} & 0 \\ 0 & v_3 (e^{-ik_x a} + e^{ik_y a}) & w_3 & 0 \\ v_3 e^{ik_y a} & 0 & v_3 e^{ik_x a} & w_3 \end{pmatrix}. \tag{10}$$

Here, the τ value is 1 or 2 for Eq. (9). The eigenvalue E, at the X point, can be derived by solving Eqs. (4) and (5), assuming that the next-nearest-neighbor coupling strength ($v_3 = 0$) can be ignored and also the coupling strengths for distant grid points;[4,23] E has eight different values, which indicates that there are eight eigenenergies (which explains the appearance of eight bands). The eigenenergies of the X point can be expressed as

$$E_{\mathrm{I}} = \pm v_1 \pm v_2 \pm \sqrt{(v_1 - v_2)^2 + w_3{}^2}, \tag{11}$$

$$E_{\mathrm{II}} = \pm w_1 \pm w_2 \pm \sqrt{(w_1 - w_2)^2 + w_3{}^2}, \tag{12}$$

where the subscript I is given 1, 3, 5, or 7, and II is 2, 4, 6, or 8; by use of these integers, each of the eighth bands of the high symmetry points are assigned to eigenenergy. When the band at the X point is degenerate, $\Delta E = E_{\mathrm{I}} - E_{\mathrm{II}} = 0$. From Eqs. (11) and (12), it is observed that the band structure meets TNS and TTS when $|w_1 - w_2| < |v_1 - v_2|$ and $|w_1 - w_2| > |v_1 - v_2|$, respectively, and the simulated calculations correspond to Fig. 2(b). When $w_1 = v_1$ and $w_2 = v_2$, the band degenerates as shown in Fig. 2(c). The calculations are consistent with the theoretical derivations, which improves the explanation of the topological phase transition mechanism for the 2D IONSL PC.

Based on a method that enables the square lattice to be shrunk and expanded to generate the TTS and TNS,[4,23] 2D IONSL PCs can be developed to tune the size of the scatterers within the inner and outer circles to generate TTS and TNS. In the simulation, a box-shaped cavity structure for the topological PC that has a 13 × 13 arrangement is constructed via TNS PCs surrounded by TTS PCs; their photonic eigenmodes and electric fields of the edge states, the corner states, and the BLSs are shown in Fig. 3.

Moreover, the local DOSs (LDOSs) are calculated through the following spectral decomposition of all the photonic eigenstates of the bulk bands:[50]

$$\rho(\boldsymbol{r}, F) = \sum_n \frac{\sigma}{\pi} \frac{\varepsilon_{(\mathbf{r})} |E^{(n)}_{(\mathbf{r})}|^2}{(F - F_n)^2 + \sigma^2}. \tag{13}$$

Here, $\sigma \to 0$ is a sufficiently small number that converges the calculation. These BLSs having the property of being distributed in pairs can be divided into different modes, which are called as the pair-partitioned BLSs. They have different distributions in the x and y directions, since the box-shaped structure is protected by its C_4 symmetry. If this structural symmetry is broken, the two different distributions of the BLSs do not arise. The frequencies of the pair-partitioned BLSs occur in an area close to that of the topological corner states. A trend that the frequencies of the multi-partitioned BLSs are higher than those of the few-partitioned BLSs is also shown, which provides more possibilities for the improved control of the BLSs. Pair-partitioned BLSs may enhance research into certain topological states at higher and lower frequencies; thus, opportunities for the discovery of topological states in the near future are expected. Such pair-partitioned BLSs at different frequencies can be divided into four cases; the principles of their generation and the corresponding electric field distributions are shown in Fig. 4.

TTS and TNS have different topological properties that produce band-inversion-induced reflections at the topological interface between the two PCs. They also form an effective cavity feedback for photon states in a small range of wave vectors around the Γ point due to the opposite parities of the wavefunctions. The states in the TTS PCs cannot propagate into the TNS PCs, and vice versa, which leads to localization of the optical field in the TNS region. Unlike on the researched photon states[35] with frequencies below the PBG and approaching to the band edges at the Γ point, this work involves the same scenario but relates to a position above the PBG. Due to a narrow PBG, the s and p_x modes couple with each other. Next, the s and p_x

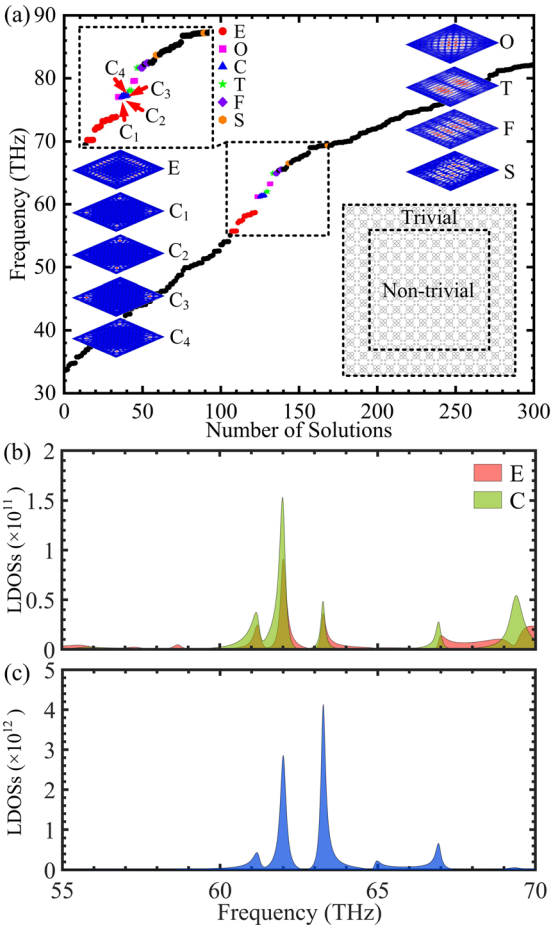

FIG. 3. (a) Graph showing the photonic eigenmodes of a box-shaped structure over the frequency range 30–90 THz. The lower-right inset depicts the box-shaped structure, in which the PC with TNS resides inside the box and the PC with TTS is outside the box. The upper-left inset displays the edge states, the corner states, one BLS, pair-two-partitioned BLSs, pair-four-partitioned BLSs, and pair-six-partitioned BLSs. These are represented by a red circle with E, blue triangle with C, carmine square with O, green pentagon with T, purple diamond with F, and orange hexagon with S. The other insets provide the electric fields for these states, including the electric fields of the four topological corner states with corresponding frequencies 61.24 THz (C_1), 61.33 THz (C_2 and C_3), and 61.43 THz (C_4). (b) Graph depicting the LDOSs of the edge states (E) and the corner states (C). (c) Graph depicting the LDOSs of the BLSs.

modes of the intra-cell and inter-cell modes, at different positions in the box-shaped structure cavity of a topological PC, are selected for the analysis depicted in Figs. 4(a), 4(e), 4(i), and 4(m). The s modes have even parities, while p_x and p_y modes have odd parities. The reasons for generation principles of BLSs are as follows: (i) There are two explanations for the one BLS. One is that the parities between the intra-cell s mode on the inside and intra-cell p_x mode at the interface are opposite and produce two reflections in the x direction, and the other is that the parities between interior s modes and interfaced p_y modes are also opposite and generate two reflections in the y direction. These two parts together lead to the one BLS as shown in Fig. 4(b). (ii) As for the pair-two-partitioned BLSs shown in Fig. 4(f), the parities

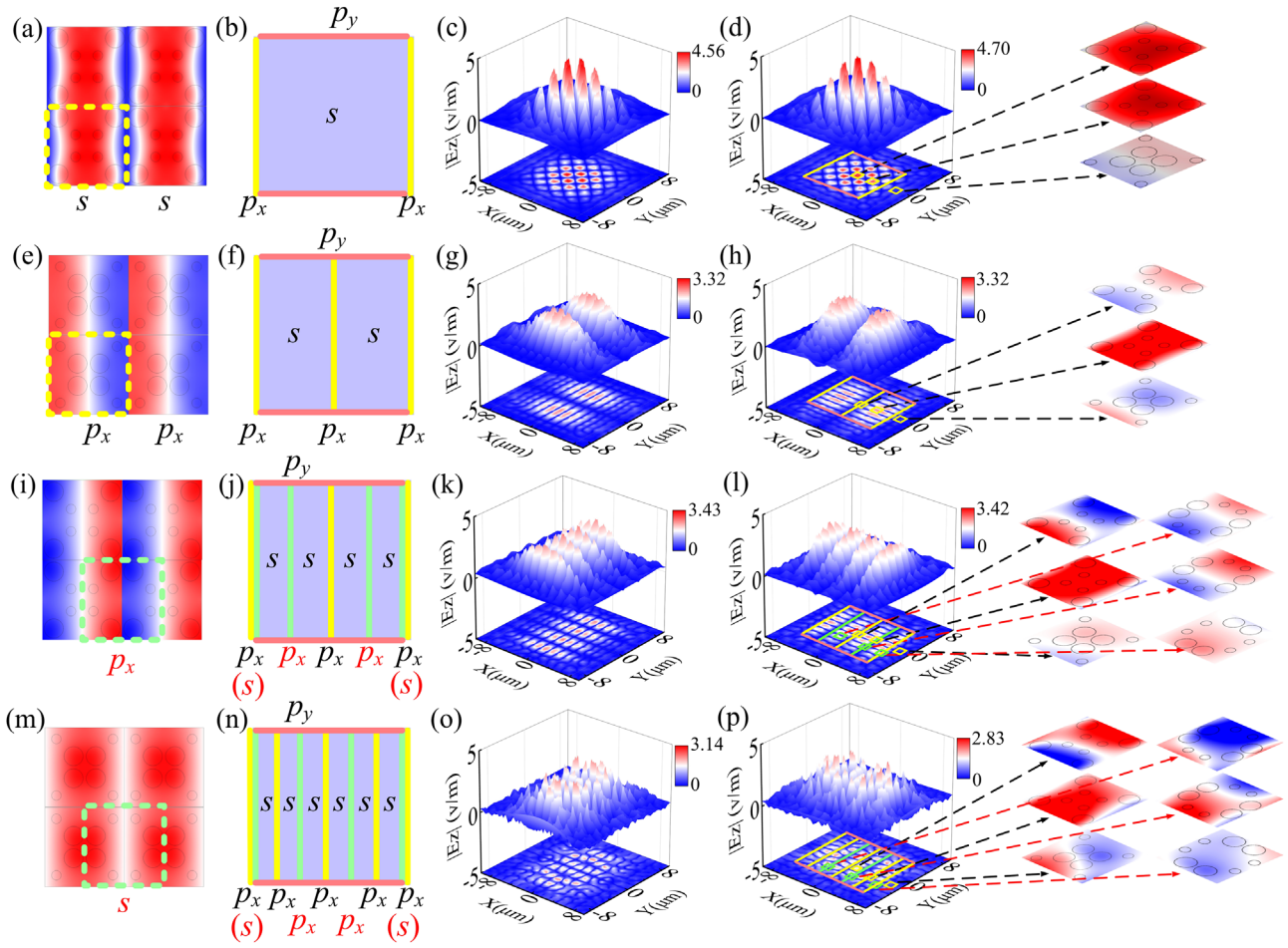

FIG. 4. Generation principles of the pair-partitioned BLSs and their electric field distributions: The optical field reflection and confinement mechanism induced by the different parity of *s*, p_x, and p_y are shown as yellow (intra-cell modes), green (inter-cell modes), and magenta (intra-cell modes) lines. (a) Intra-cell *s* mode with even parity. (b) Analytical of one BLS and (c) and (d) one BLS that corresponds to 61.21 THz. (e) Intra-cell p_x mode with odd parity. (f) Analytical of pair-two-partitioned BLSs and (g) and (h) pair-two-partitioned BLSs that relate to 62.01 THz. (i) Inter-cell p_x mode with even parity. (j) Analytical of pair-four-partitioned BLSs and (k) and (l) pair-four-partitioned BLSs at 64.92 THz. (m) Intra-cell *s* mode with odd parity. (n) Analytical of pair-six-partitioned BLSs and (o) and (p) pair-six-partitioned BLSs at 69.37 THz.

between intra-cell p_x modes at the central position and the interface, and the intra-cell *s* modes at the left and right positions are opposite, indicating the occurrence of three reflections in the *x* direction, which together with the two reflections in the *y* direction lead to the pair-two-partitioned BLSs. (iii) On introducing inter-cell *s* and p_x modes, account for the four-partitioned BLSs can be explained by the mode coupling. The inversions of the intra-cell *s* and p_x modes, with inter-cell *s* and p_x modes, lead to five reflections in the *x* direction, which obtains the pair-four-partitioned BLSs together with two reflections in the *y* direction as shown in Fig. 4(j). (iv) Compared to four-partitioned BLSs, the distinct parities of *s* and p_x modes have added two reflections, resulting in pair-six-partitioned BLSs as shown in Fig. 4(n). The electric field distributions of the various partitions are shown in Figs. 4(c), 4(d), 4(g), 4(h), 4(k), 4(l), 4(o), and 4(p), which exhibit the different electric fields for the partitioned BLSs with the TNS in the box-shaped structure. The close agreement of the computational and theoretical results confirms the principles for generation of pair-partitioned BLSs, and it is also shown that the BLSs can have a diverse range of forms.

In summary, we propose a cavity of topological PCs with 2D IONSL in this Letter. The relationship between the size of scatterers in the inner and outer circles within the unit cell and the TTS and TNS is analyzed. The relevant Hamiltonian is derived based on an analogous tight-binding model used for an electronic system. This further verifies the topological phase transition and connects the bulk polarization to the Zak phase. Subsequently, the pair-partitioned BLSs that are induced by topological band inversions are realized in the box-shaped structure cavity of the topological PC. The relationship between the eigenfrequency and the electric field distribution of the pair-partitioned BLSs is also analyzed. This work provides ideas in relation to the potential production of topological bulk lasers. Moreover, it demonstrates the existence of bulk topological effects beyond the regularly studied edge states and corner states and can also be applicable for VCSELs.

The authors acknowledge the financial support from the National Natural Science Foundation of China (Grant Nos. 61405058 and 62075059), the Natural Science Foundation of Hunan Province (Grant Nos. 2017JJ2048 and 2020JJ4161), and the Fundamental Research Funds for the Central Universities (Grant No. 531118040112). The authors thank Professor J. Liu for software sponsorship.

AUTHOR DECLARATIONS

Conflict of Interest

The authors have no conflicts to disclose.

Author Contributions

Peng Peng: Data curation (lead); Formal analysis (supporting); Investigation (lead); Methodology (supporting); Software (lead); Writing – original draft (lead); Writing – review and editing (lead). **Exian Liu:** Formal analysis (supporting); Investigation (supporting); Methodology (supporting); Software (supporting). **Bei Yan:** Formal analysis (supporting); Investigation (supporting); Methodology (supporting); Software (supporting). **Yuchen Peng:** Formal analysis (supporting); Investigation (supporting); Methodology (supporting); Software (supporting). **Aoqian Shi:** Formal analysis (supporting); Investigation (supporting); Methodology (supporting); Software (supporting). **Jianlan Xie:** Formal analysis (supporting); Investigation (supporting); Methodology (supporting); Software (supporting). **Hang Li:** Formal analysis (supporting); Investigation (supporting); Methodology (supporting); Software (supporting). **Yuanjiang Xiang:** Formal analysis (supporting); Investigation (supporting); Methodology (supporting); Software (supporting). **Jianjun Liu:** Conceptualization (lead); Formal analysis (lead); Funding acquisition (lead); Methodology (lead); Project administration (lead); Resources (lead); Supervision (lead); Validation (lead).

DATA AVAILABILITY

The data that support the findings of this study are available within the article.

REFERENCES

[1]B. Xie, H. Wang, X. Zhu, M. Lu, Z. D. Wang, and Y. Chen, "Photonics meets topology," Opt. Express **26**(19), 24531–24550 (2018).
[2]T. Ozawa, H. M. Price, A. Amo, N. Goldman, M. Hafezi, L. Lu, M. C. Rechtsman, D. Schuster, J. Simon, O. Zilberberg, and I. Carusotto, "Topological photonics," Rev. Mod. Phys. **91**(1), 015006 (2019).
[3]M. Jung, R. G. Gladstone, and G. B. Shvets, "Nanopolaritonic second-order topological insulator based on graphene plasmons," Adv. Photonics **2**(4), 046003 (2020).
[4]X. Chen, W. Deng, F. Shi, F. Zhao, M. Chen, and J. Dong, "Direct observation of corner states in second-order topological photonic crystal slabs," Phys. Rev. Lett. **122**(23), 233902 (2019).
[5]B. Xie, G. Su, H. Wang, H. Su, X. Shen, P. Zhan, M. Lu, Z. Wang, and Y. Chen, "Visualization of higher-order topological insulating phases in two-dimensional dielectric photonic crystals," Phys. Rev. Lett. **122**(23), 233903 (2019).
[6]M. Serra-Garcia, V. Peri, R. Süsstrunk, O. R. Bilal, T. Larsen, L. G. Villanueva, and S. D. Huber, "Observation of a phononic quadrupole topological insulator," Nature **555**(7696), 342–345 (2018).
[7]Z. Zhang, M. Rosendo López, Y. Cheng, X. Liu, and J. Christensen, "Non-Hermitian sonic second-order topological insulator," Phys. Rev. Lett. **122**(19), 195501 (2019).
[8]T. Liu, Y. R. Zhang, Q. Ai, Z. Gong, K. Kawabata, M. Ueda, and F. Nori, "Second-order topological phases in non-Hermitian systems," Phys. Rev. Lett. **122**(7), 076801 (2019).
[9]B. Yan, J. Xie, E. Liu, Y. Peng, R. Ge, J. Liu, and S. Wen, "Topological edge state in the two-dimensional Stampfli-triangle photonic," Phys. Rev. Appl. **12**(4), 044004 (2019).
[10]Y. Peng, B. Yan, J. Xie, E. Liu, H. Li, R. Ge, F. Gao, and J. Liu, "Variation of topological edge states of 2D honeycomb lattice photonic crystals," Phys. Status Solidi RRL **14**(9), 2000202 (2020).
[11]M. C. Rechtsman, J. M. Zeuner, Y. Plotnik, Y. Lumer, D. Podolsky, F. Dreisow, S. Nolte, M. Segev, and A. Szameit, "Photonic Floquet topological insulators," Nature **496**(7444), 196–200 (2013).
[12]A. B. Khanikaev, S. Hossein Mousavi, W. K. Tse, M. Kargarian, A. H. MacDonald, and G. Shvets, "Photonic topological insulators," Nat. Mater. **12**(3), 233–239 (2013).
[13]W. Gao, B. Yang, B. Tremain, H. Liu, Q. Guo, L. Xia, A. P. Hibbins, and S. Zhang, "Experimental observation of photonic nodal line degeneracies in metacrystals," Nat. Commun. **9**(1), 950 (2018).
[14]Q. Yan, R. Liu, Z. Yan, B. Liu, H. Chen, Z. Wang, and L. Lu, "Experimental discovery of nodal chains," Nat. Phys. **14**(5), 461–464 (2018).
[15]D. D. Solnyshkov, O. Bleu, and G. Malpuech, "Topological optical isolator based on polariton graphene," Appl. Phys. Lett. **112**(3), 031106 (2018).
[16]M. P. Makwana and G. Chaplain, "Tunable three-way topological energy-splitter," Sci. Rep. **9**(1), 18939 (2019).
[17]W. Song, W. Sun, C. Chen, Q. Song, S. Xiao, S. Zhu, and T. Li, "Robust and broadband optical coupling by topological waveguide arrays," Laser Photonics Rev. **14**(2), 1900193 (2020).
[18]X. Yin, J. Jin, M. Soljačić, C. Peng, and B. Zhen, "Observation of topologically enabled unidirectional guided resonances," Nature **580**(7804), 467–471 (2020).
[19]M. Ezawa, "Higher-order topological insulators and semimetals on the breathing kagome and pyrochlore lattices," Phys. Rev. Lett. **120**(2), 026801 (2018).
[20]B. Xie, H. Wang, H. Wang, X. Zhu, J. Jiang, M. Lu, and Y. Chen, "Second-order photonic topological insulator with corner states," Phys. Rev. B **98**(20), 205147 (2018).
[21]H. Hu, B. Huang, E. Zhao, and W. V. Liu, "Dynamical singularities of Floquet higher-order topological insulators," Phys. Rev. Lett. **124**(5), 057001 (2020).
[22]C. W. Peterson, T. Li, W. A. Benalcazar, T. L. Hughes, and G. Bahl, "A fractional corner anomaly reveals higher-order topology," Science **368**(6495), 1114–1118 (2020).
[23]W. Zhang, X. Xie, H. Hao, J. Dang, S. Xiao, S. Shi, H. Ni, and Z. Niu, "Low-threshold topological nanolasers based on the second-order corner state," Light Sci. Appl. **9**(1), 109 (2020).
[24]M. Li, D. Zhirihin, M. Gorlach, X. Ni, D. Filonov, A. Slobozhanyuk, A. Alù, and A. B. Khanikaev, "Higher-order topological states in photonic kagome crystals with long-range interactions," Nat. Photonics **14**(2), 89–94 (2020).
[25]H. R. Kim, M. S. Hwang, D. Smirnova, K. Y. Jeong, Y. Kivshar, and H. G. Park, "Multipolar lasing modes from topological corner states," Nat. Commun. **11**(1), 5758 (2020).
[26]B. Xie, G. Su, H. F. Wang, F. Liu, L. Hu, S. Y. Yu, P. Zhan, M. H. Lu, Z. Wang, and Y. F. Chen, "Higher-order quantum spin Hall effect in a photonic crystal," Nat. Commun. **11**(1), 3768 (2020).
[27]M. Kim and J. Rho, "Topological edge and corner states in a two-dimensional photonic Su–Schrieffer–Heeger lattice," Nanophotonics **9**(10), 3227–3234 (2020).
[28]B. Xie, H. X. Wang, X. Zhang, P. Zhan, J. H. Jiang, M. Lu, and Y. Chen, "Higher-order band topology," Nat. Rev. Phys. **3**(7), 520–532 (2021).
[29]J. Noh, W. A. Benalcazar, S. Huang, M. J. Collins, K. P. Chen, T. L. Hughes, and M. C. Rechtsman, "Topological protection of photonic mid-gap defect modes," Nat. Photonics **12**(7), 408–415 (2018).
[30]F. F. Li, H. X. Wang, Z. Xiong, Q. Lou, P. Chen, R. X. Wu, Y. Poo, J. H. Jiang, and S. John, "Topological light-trapping on a dislocation," Nat. Commun. **9**(1), 2462 (2018).
[31]X. Xie, W. Zhang, X. He, S. Wu, J. Dang, K. Peng, F. Song, L. Yang, H. Ni, Z. Niu, C. Wang, K. Jin, X. Zhang, and X. Xu, "Cavity quantum electrodynamics with second-order topological corner state," Laser Photonics Rev. **14**(8), 1900425 (2020).

[32]D. Smirnova, A. Tripathi, S. Kruk, M. S. Hwang, H. R. Kim, H. G. Park, and Y. Kivshar, "Room-temperature lasing from nanophotonic topological cavities," Light: Sci. Appl. **9**(1), 127 (2020).
[33]X. Xie, S. Yan, J. Dang, J. Yang, S. Xiao, Y. Wang, S. Shi, L. Yang, D. Dai, Y. Yuan, N. Luo, T. Cui, G. Chi, Z. Zuo, B. B. Li, C. Wang, and X. Xu, "Topological cavity based on slow-light topological edge mode for broadband Purcell enhancement," Phys. Rev. Appl. **16**(1), 014036 (2021).
[34]A. Shi, B. Yan, R. Ge, J. Xie, Y. Peng, H. Li, W. E. I. Sha, and J. Liu, "Coupled cavity-waveguide based on topological corner state and edge state," Opt. Lett. **46**(5), 1089–1092 (2021).
[35]Z. Shao, H. Chen, S. Wang, X. Mao, Z. Yang, S. Wang, X. Wang, X. Hu, and R. Ma, "A high-performance topological bulk laser based on band-inversion-induced reflection," Nat. Nanotechnol. **15**(1), 67–72 (2020).
[36]D. Mahgerefteh and C. Thompson, "Techno-economic comparison of silicon photonics and multimode VCSELs," J. Lightwave Technol. **34**(2), 233–242 (2016).
[37]H. Lin, S. Ourari, T. Huang, A. Jha, A. Briggs, and N. Bigagli, "Photonic microwave generation in multimode VCSELs subject to orthogonal optical injection," J. Opt. Soc. Am. B **34**(11), 2381–2389 (2017).
[38]W. Yang, G. Xia, E. Jayaprasath, Z. Jiang, Y. Hou, C. Hu, and Z. Wu, "Experimental investigation on the nonlinear dynamics of two mutually coupled 1550 nm multi-transverse-mode vertical-cavity surface-emitting lasers," Appl. Opt. **58**(5), 1271–1275 (2019).
[39]D. Obana, F. Liu, and K. Wakabayashi, "Topological edge states in the Su–Schrieffer–Heeger model," Phys. Rev. B **100**(7), 075437 (2019).
[40]B. Yan, Y. Peng, A. Shi, J. Xie, P. Peng, and J. Liu, "Pseudo-spin-valley coupled topological states protected by different symmetries in photonic crystals," Opt. Lett. **47**(8), 2044–2047 (2022).
[41]J. Jiang, B. Yan, Y. Peng, J. Xie, A. Shi, and J. Liu, "Multiband topological states in non-Hermitian photonic crystals," Opt. Lett. **47**(2), 437–440 (2022).
[42]C. Lu, C. Wang, M. Xiao, Z. Q. Zhang, and C. T. Chan, "Topological rainbow concentrator based on synthetic dimension," Phys. Rev. Lett. **126**(11), 113902 (2021).
[43]M. L. N. Chen, L. J. Jiang, Z. Lan, and W. E. I. Sha, "Pseudospin-polarized topological line defects in dielectric photonic crystals," IEEE Trans. Antennas Propag. **68**(1), 609–613 (2020).
[44]Y. Wei, B. Yan, Y. Peng, A. Shi, D. Zhao, R. Peng, Y. Xiang, and J. Liu, "Fragile topology in double-site honeycomb lattice photonic crystal," Opt. Lett. **46**(16), 3941–3944 (2021).
[45]Z. Zhang, H. Long, C. Liu, C. Shao, Y. Cheng, X. Liu, and J. Christensen, "Deep-subwavelength holey acoustic second-order topological insulators," Adv. Mater. **31**(49), 1904682 (2019).
[46]C. Fang, M. J. Gilbert, and B. A. Bernevig, "Bulk topological invariants in non-interacting point group symmetric insulators," Phys. Rev. B **86**(11), 115112 (2012).
[47]J. M. Lourtioz, H. Benisty, V. Berger, J. M. Gérard, D. Maystre, and A. Tchelnokov, *Photonic Crystals: Towards Nanoscale Photonic Devices* (Springer-Verlag, Berlin, 2008), pp. 59–77.
[48]I. A. Sukhoivanov and I. V. Guryev, *Photonic Crystals: Physics and Practical Modeling* (Springer-Verlag, Berlin, 2009), pp. 96–103.
[49]L. Xu, H. Wang, Y. Xu, H. Chen, and J. Jiang, "Accidental degeneracy in photonic bands and topological phase transitions in two-dimensional core-shell dielectric photonic crystals," Opt. Express **24**(16), 18059–18071 (2016).
[50]H. X. Wang, L. Liang, B. Jiang, J. Hu, X. Lu, and J. H. Jiang, "Higher-order topological phases in tunable C_3 symmetric photonic crystals," Photonics Res. **9**(9), 1854–1864 (2021).